

Exploration Geophysics



ISSN: 0812-3985 (Print) 1834-7533 (Online) Journal homepage: https://www.tandfonline.com/loi/texg20

First-arrival tomography with fast sweeping method solving the factored eikonal equation

Guangnan Huang, Songting Luo, Tryggvason Ari, Hongxing Li & David C. Nobes

To cite this article: Guangnan Huang, Songting Luo, Tryggvason Ari, Hongxing Li & David C. Nobes (2019) First-arrival tomography with fast sweeping method solving the factored eikonal equation, Exploration Geophysics, 50:2, 144-158, DOI: 10.1080/08123985.2019.1577110

To link to this article: https://doi.org/10.1080/08123985.2019.1577110

	Published online: 26 Feb 2019.
	Submit your article to this journal 🗷
ılıl	Article views: 16
CrossMark	View Crossmark data 🗗





First-arrival tomography with fast sweeping method solving the factored eikonal equation

Guangnan Huang^{a,b,c}, Songting Luo^c, Tryggvason Ari^d, Hongxing Li^{a,b} and David C. Nobes^{a,b}

^aState Key Laboratory of Nuclear Resources and Environment, East China University of Technology, Nanchang, China; ^bDepartment of Geophysics, East China University of Technology, Nanchang, China; Cpepartment of Mathematics, Iowa State University, Ames, IA, USA; ^dDepartment of Earth Science, Uppsala University, Uppsala, Sweden

This paper presents a first-arrival tomography incorporating a fast sweeping method (FSM) solving the factored eikonal equation (factored FSM). The traveltime calculation method plays a significant role in velocity inversion. However, for a point source condition, all finite-difference based eikonal solvers suffer from the source singularity problem. Numerical error caused by source singularity will propagate from the source to all computational domains, and makes traveltimes inaccurate. A FSM solving the factored eikonal equation can deal with the source singularity problem very well. Therefore, a first-arrival tomography is developed by incorporating 2D and 3D factored FSMs to provide more accurate traveltimes in velocity inversion. For comparison, an open source package PStomo_eq is used to invert the same data set. It incorporates the traveltime calculation algorithms fdtime2d.c and fdtime3d.c. Traveltime accuracy tests show that factored FSM can generate more accurate traveltimes than FSM, fdtime2d.c and fdtime3d.c. Numerical and field data tests show that inversion with factored FSM can acquire much better tomograms than inversion with fdtime2d.c and fdtime3d.c. Therefore, it is worthwhile using a more accurate traveltime computation method in velocity inversion.

ARTICLE HISTORY

Received 16 June 2018 Accepted 25 January 2019

KEYWORDS

seismic tomography; fast sweeping method; factored eikonal equation

Introduction

Seismic traveltime tomography can invert a few parameters (velocity of longitudinal wave and shear wave, quality factor, anisotropic parameters, etc.) by use of large numbers of arrival times. In seismology and geodynamics, earth structures can be obtained by use of seismic events received continuously from stations (Aki and Lee 1976; Engdahl, Hilst, and Buland 1998). Velocity information can be used to investigate oceanic ridges, continental plate subduction zones, volcanic channels, geological faults, and the interface between the mantle and the core (Lees 1992; Kennett, Engdahl, and Buland 1995; Calvert and Fisher 2001; Rawlinson and Fishwick 2012). In resource exploration, seismic traveltime tomography is used successfully in exploring oil and gas reservoirs, coal and nonferrous metal deposits. Statics and seismic migration rely greatly on an accurate velocity model which can be obtained from traveltime tomography (Vesnaver et al. 2003; Bergman, Tryggvason, and Juhlin 2004; Zhou 2006). In engineering investigations, seismic traveltime tomography is used widely in the detection of dam water leakage and underground water pollution, foundation investigations, etc. (Ajo-Franklin, Urban, and Harris 2006; Zelt, Azaria, and Levander 2006; Marti, Carbonell, and Flecha 2008).

Methods of traveltime computation are well developed, for example, the shooting and bending method, shortest path method, wavefront reconstruction method and finite-difference based eikonal solver. The ray-tracing method can provide accurate traveltimes, but it is difficult to pass through shadow zones when the model is complicated (Cerveny 2001). The shortest path method is based on graph theory (Nakanishi and Yamaguchi 1986; Moser 1991; Fischer and Lees 1993; Zhou and Greenhalgh 2006; Huang et al. 2014, 2017). It has good numerical stability, but low accuracy and efficiency (Cheng and House 1996; Leidenfrost et al. 1999). The wavefront reconstruction method uses a local raytracing method for the current wavefront repeatedly to obtain a new wavefront, until all traveltimes are computed for the whole computational domain (Vinje, Iversen, and Gjoystdal 1993, 1999; Ettrich and Gajewski 1996; Lambare, Lucio, and Hanyga 1996). This method costs too much in terms of computational time for the same level of accuracy, compared with the finitedifference based eikonal solver (Leidenfrost et al. 1999). The eikonal solver is the most promising method. Vidale (1988, 1990) is a pioneer of the use of a finite-difference scheme to calculate traveltimes. This method has been developed and modified further by many geophysicists (Podvin and Lecomte 1991; Van Trier and Symes 1991; Qin, Luo, and Olsen 1992; Hole and Zelt 1995; Kim and Cook 1999). Among these methods, the fast-marching method (FMM) (Sethian and Popovici 1999) and fast sweeping method (FSM) (Tsai Cheng, Osher, and Zhao 2003; Zhao 2005) are the most promising. FMM incorporates an upwind finite-difference scheme, narrow-band technique and heap-sorting algorithm to describe wavefront expansion. Its computational complexity is O(NlogN), where N is total number of grid points. FSM is an iterative method. It incorporates an upwind finite-difference scheme and Gauss–Seidel iteration with alternating sweeping orderings. Its computational complexity is O(N).

There are two important features in seismic traveltime tomography: (1) the traveltime computation method; and (2) a regularised inversion algorithm to reduce the discrepancy between observed and calculated traveltimes. Therefore, traveltime accuracy is very important in seismic traveltime tomography. For a point source condition, traveltimes calculated by eikonal solver suffer from the source singularity problem (Qian and Symes 2002a; Waheed and Alkhalifah 2017). The numerical error of a finite-difference approximation near the source point is very large. This error can spread from the source to the whole computational domain and renders all finite-difference based eikonal solvers first-order convergence at most. One approach to dealing with the source singularity problem is to set a homogeneous velocity block near the source point to calculate analytical solutions for these points (Qian and Symes 2001; Han, Zhang, and Zhang 2017). Another approach is to refine the grid near the source point to reduce large truncation errors (Kim and Cook 1999; Qian and Symes 2002b). Fomel, Luo, and Zhao (2009) proposed a FSM to solve the factored eikonal equation, which deals with the source singularity problem very well.

Here, we introduce a FSM to solve 2D and 3D factored eikonal equations. It breaks down the solution of the eikonal equation into two factors: one factor is calculated analytically, and the other is a necessary modification (smoothing) in the neighbourhood of the source point. For comparison, we use the *PStomo_eq* program to implement velocity inversion incorporating *fdtime2d.c* and *fdtime3d.c*. 2D and 3D factored FSMs are used to replace *fdtime2d.c* and *fdtime3d.c* in *PStomo_eq* to provide more accurate traveltimes for velocity inversion. The traveltimes of P- and S-waves are used in traveltime tomography to resolve the non-uniqueness of the inverse problem.

The remainder of this paper is organised as follows: (1) We introduce the methodology of seismic traveltime tomography, factored FSM and the principle of *fdtime2d.c* are also recalled briefly. (2) An analytical solution and traveltimes calculated using the factored FSMs, FSMs, *fdtime2d.c* and *fdtime3d.c* of a constant gradient

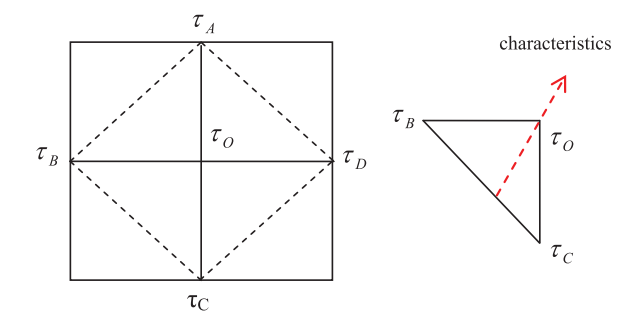


Figure 1. 2D rectangular mesh.

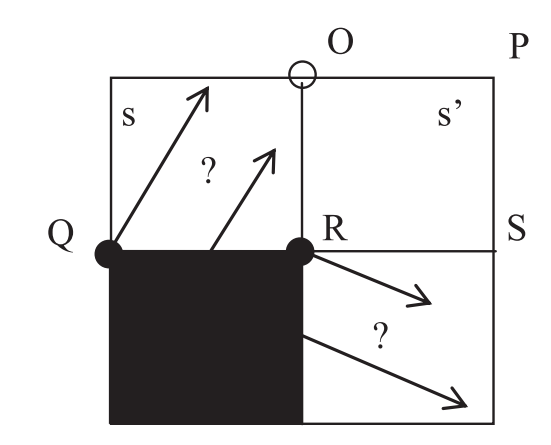


Figure 2. Traveltime calculation for transmission wave. *s* and *s'* are the slowness of the current cell and its adjacent cell.

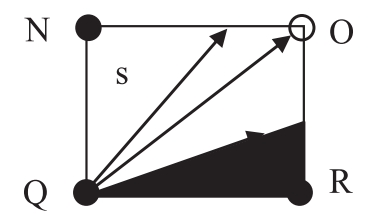


Figure 3. Traveltime calculation for diffracted waves. A local shadow zone is presented and corner Q acts as a secondary source.

velocity model are used for comparison. (3) 2D and 3D factored FSMs, *fdtime2d.c* and *fdtime3d.c* are used in the *PStomo_eq* program to invert 2D and 3D checkerboard velocity models. (4) the *PStomo_eq* program incorporating different traveltime computation algorithms is used to invert 2D and 3D field data sets. (5) Conclusions are drawn about factored FSM and its application in numerical and field examples.

Methodology

Seismic traveltime tomography

Linearisation and discretisation are used in seismic traveltime tomography (Lees and Crosson 1989). The computational domain is often discretised with a certain mesh size. The slowness of each cell or grid is assumed to be constant. The ray path and traveltime for each source and receiver pair can be calculated after the

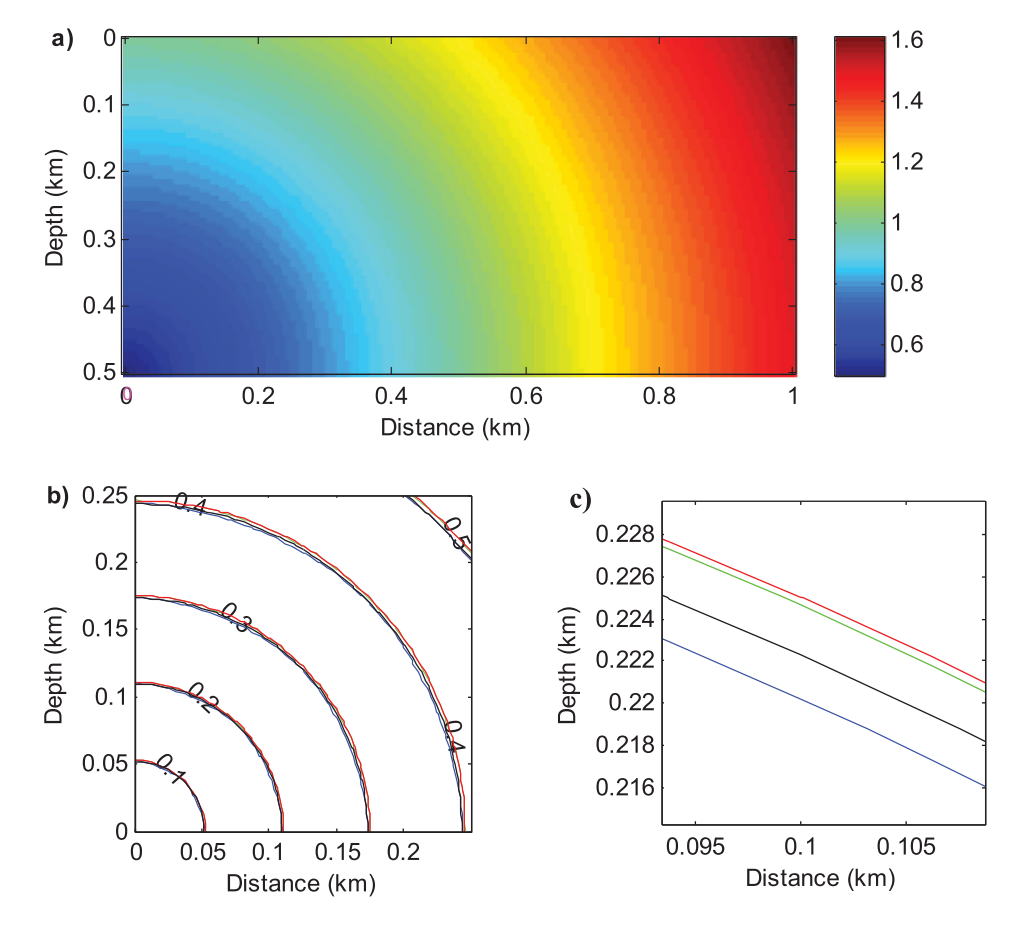


Figure 4. Traveltime accuracy test for a 2D velocity model. (a) 2D constant gradient velocity model. (b) Traveltime contour map: green line, analytical solution; red line, traveltimes computed by factored FSM; black line, traveltimes calculated by FSM; blue line, traveltimes calculated by *fdtime2d.c.*

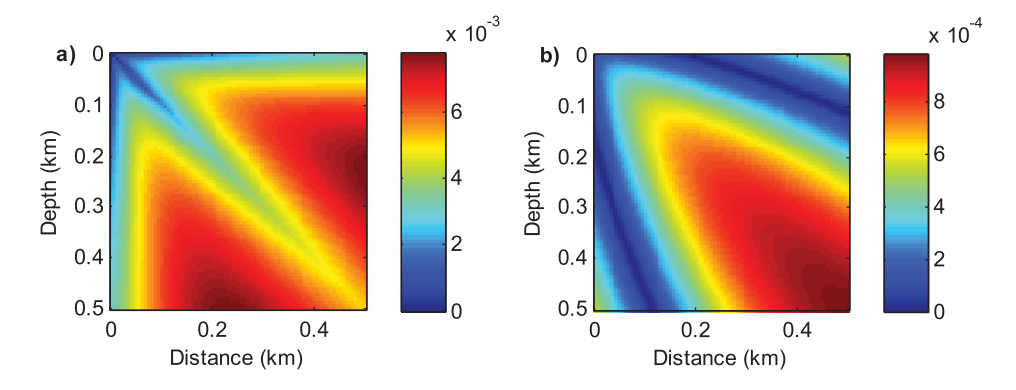


Figure 5. Traveltime differences for a 2D case. (a) Discrepancy between traveltimes calculated using an analytical solution and traveltimes computed by *fdtime2d.c* code. (b) Discrepancy between traveltimes calculated using an analytical solution and traveltimes computed by factored FSM.

source and receiver have been specified. According to inverse theory, traveltime perturbation is the integral of slowness perturbation along the ray path. Therefore, traveltime perturbation b_i can be written as a linearised equation $b_i = \sum a_{ij}x_j$, where a_{ij} is the ray length of the ith ray through the jth cell, and x_j is slowness perturbation in the jth cell. When there are a large number of source and receiver pairs, a large and sparse system of linearised equations can be used to express the seismic traveltime tomographic equation (Nolet 2008):

The damping least-square solution of Equation (1) can be expressed by an inverse matrix (Phillips and Fehler 1991):

$$\mathbf{A}_{\mathbf{q}}^{-1} = (\mathbf{A}^{\mathsf{T}}\mathbf{A} + \lambda \mathbf{I})^{-1}\mathbf{A}^{\mathsf{T}},\tag{2}$$

where **I** is the identity matrix, λ is the damping factor and $\mathbf{A}_{\mathbf{q}}^{-1}$ is the inverse of matrix $\mathbf{A}_{\mathbf{g}}$.

The observed data should be weighted by the reciprocal of estimation errors. Therefore, Equation (2) can be further written as:

$$\mathbf{A}\mathbf{x} = \mathbf{b}, \qquad \qquad \mathbf{A}_{\alpha}^{-1} = (\mathbf{A}^{T}\mathbf{C}_{d}^{-1}\mathbf{A} + \lambda \mathbf{I})^{-1}\mathbf{A}^{T}\mathbf{C}_{d}^{-1}, \qquad (3)$$

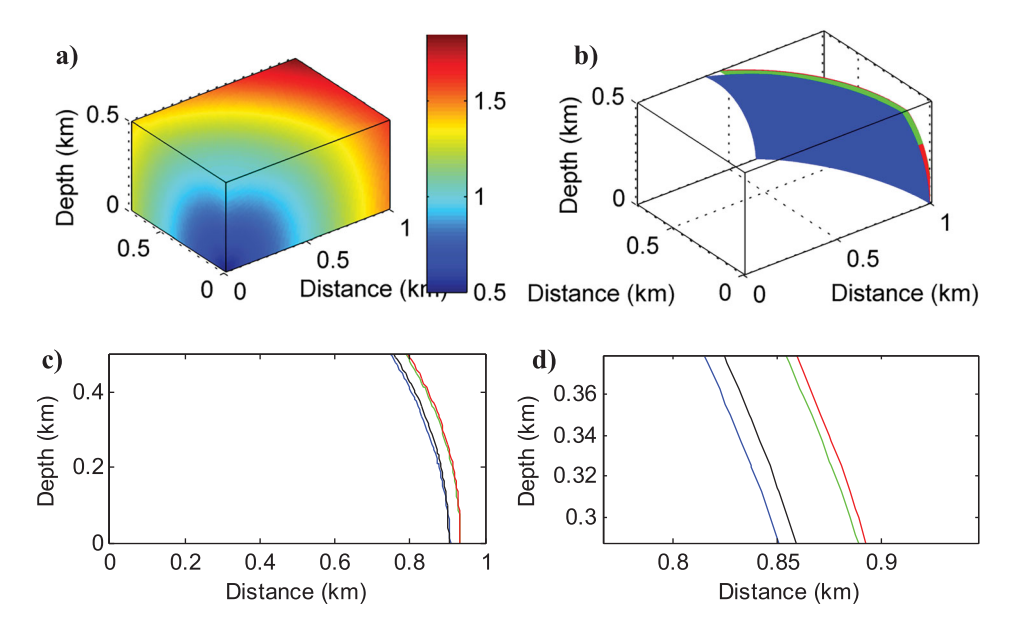


Figure 6. Traveltime accuracy test for a 3D case. (a) 3D constant gradient velocity model. (b) 3D traveltime iso-surfaces at 1.1s. (c,d) Vertical slice of 3D traveltimes and its expanded map: green line, analytical solution; red line, traveltimes computed by factored FSM; black line, traveltimes calculated by FSM; blue line, traveltimes calculated by fdtime3d.c.

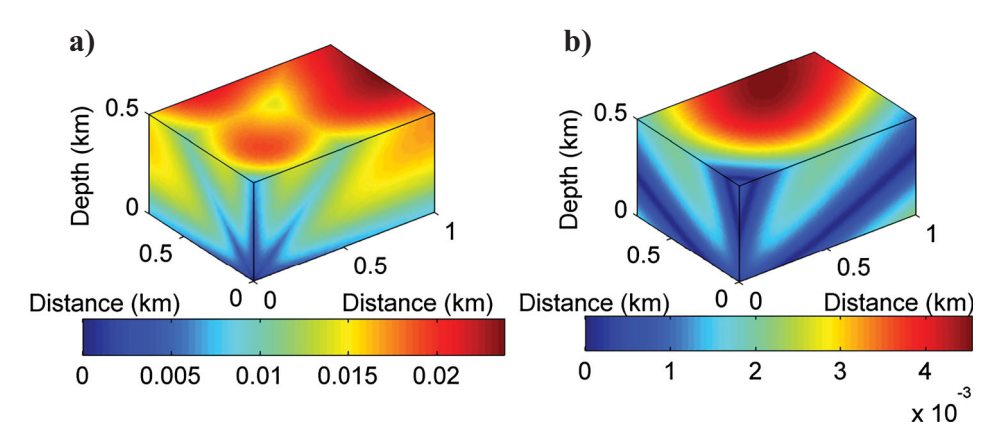


Figure 7. Traveltime differences for a 3D case. (a) Discrepancy between traveltimes calculated using an analytical solution and traveltimes computed by fdtime3d.c. (b) Discrepancy between travel times calculated using an analytical solution and travel times computedby factored FSM.

where \boldsymbol{C}_d^{-1} is a diagonal matrix. Diagonal elements of this matrix are variance in estimation errors. In order to suppress high wavenumber noises, a smoothness constraint operator is also added in the regularisation equation (Lees and Crosson 1989; Toomey, Solomon, and Purdy 1994; Tryggvason, Rognvaldsson, and Flovenz 2002). Therefore, the inversion expression and its matrix form can be written as:

$$\mathbf{A}_{a}^{-1} = (\mathbf{A}^{T} \mathbf{C}_{d}^{-1} \mathbf{A} + \lambda \mathbf{D})^{-1} \mathbf{A}^{T} \mathbf{C}_{d}^{-1}, \tag{4}$$

and

$$\begin{bmatrix} \mathbf{C}_d^{-1/2} \mathbf{A} \\ \lambda \mathbf{D} \end{bmatrix} \mathbf{x} = \begin{bmatrix} \mathbf{C}_d^{-1/2} b \\ 0 \end{bmatrix}, \tag{5}$$

where **D** is the smoothness constraint operator. Lees and Crosson (1989) explained that the smoothness constraint operator is a constraint condition for the roughness of the model. The smoothness constraint equation

of the ith cell in a 2D model can be expressed as:

$$4x_{j} - (x_{j+1} + x_{j-1} + x_{j+n} + x_{j-n}) = 0.$$
 (6)

where x_i is the slowness perturbation of the *i*th cell, and n is the cell number in each row. In order to obtain a reasonable velocity model, we also specify the upper and lower bounds of the velocity model (Zhou, Sinadinovski, and Greenhalgh 1992). These methods and equations are adopted in the PStomo eq package.

Fast sweeping method solving the factored eikonal equation

For a point source condition, there is a source singularity problem when a finite-difference scheme is used to solve the eikonal equation. In order to resolve the source singularity problem, a factorisation method is introduced (Fomel, Luo, and Zhao 2009; Luo and Qian 2011, 2012). Here, the factorisation method is recalled briefly.

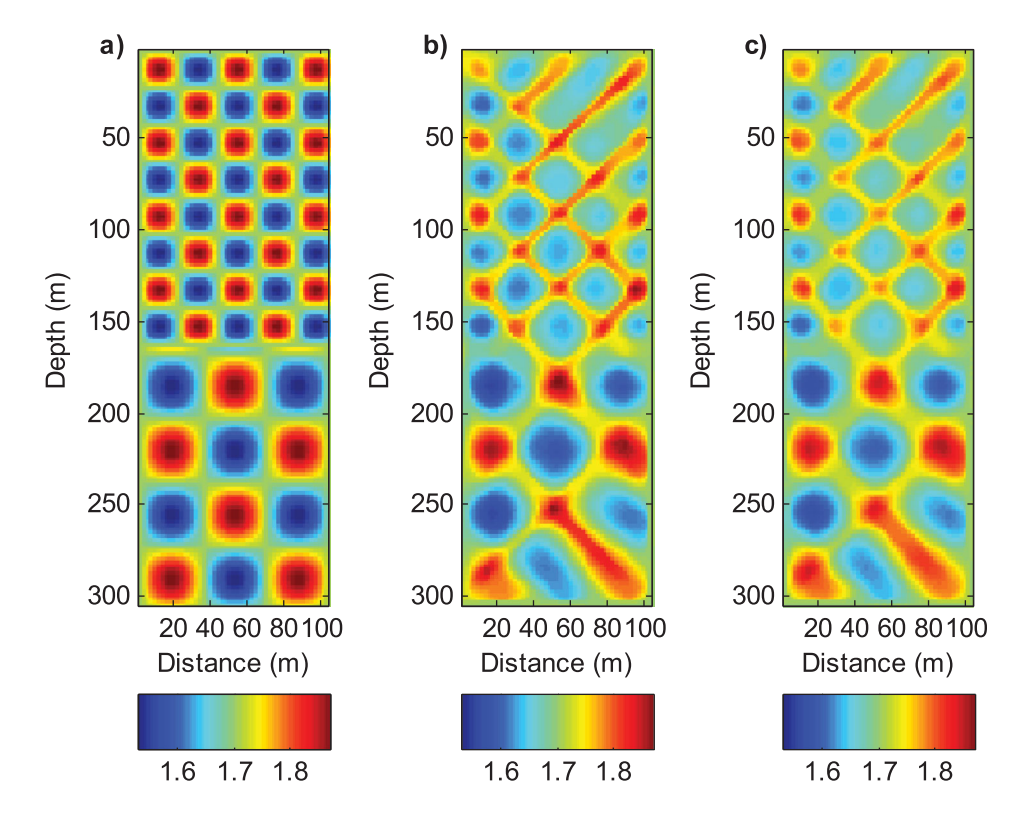


Figure 8. 2D inversion results for comparison of the P-wave. (a) P-wave checkerboard model. (b) Inversion with factored FSM. (c) Inversion with *fdtime2d.c*.

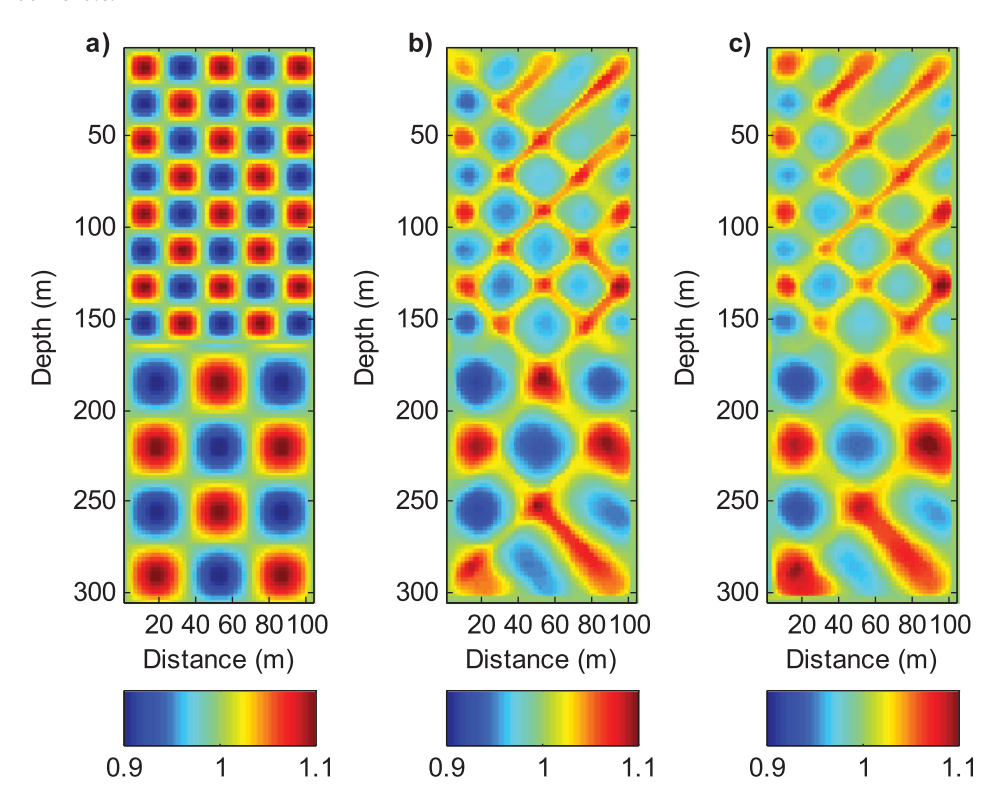


Figure 9. 2D inversion results for comparison of the S-wave. (a) S-wave checkerboard model. (b) Inversion with factored FSM. (c) Inversion with fdtime2d.c.

The eikonal equation

$$|\nabla T(\mathbf{x})|^2 = S^2(\mathbf{x}), \mathbf{x} \in R^n, \tag{7}$$

describes traveltime $T(\mathbf{x})$ propagating in a slowness model $S(\mathbf{x})$, in space $\mathbf{x} \in R^n$. We break down the solution of eikonal equation into two factors: one is calculated

analytically or numerically, and the other is a necessary modification in the neighbourhood of the source point. For Equation (7), it can be broken down as

$$S(\mathbf{x}) = S_0(\mathbf{x})\alpha(\mathbf{x}),\tag{8}$$

$$T(\mathbf{x}) = T_0(\mathbf{x})\tau(\mathbf{x}),\tag{9}$$

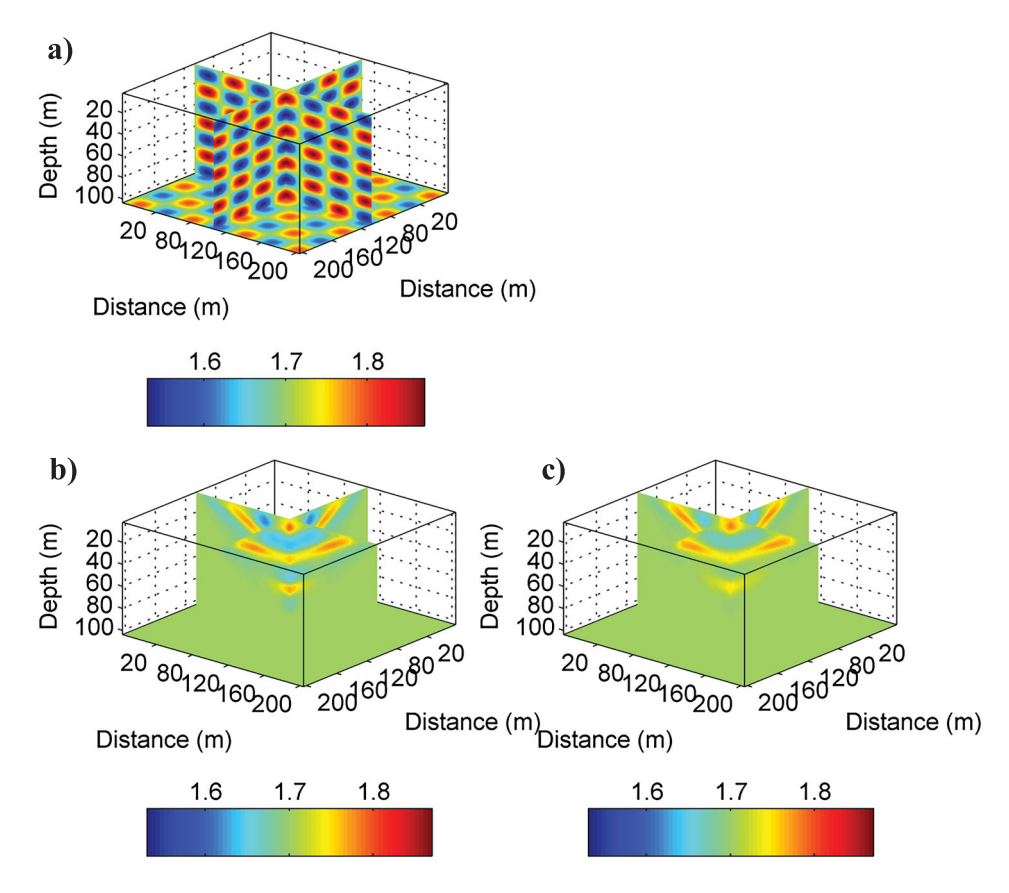


Figure 10. 3D inversion results comparison of P-wave. (a) P-wave checkerboard velocity model. (b) Result obtained by inversion with 3D factored FSM. (c) Result obtained by inversion with fdtime3d.c.

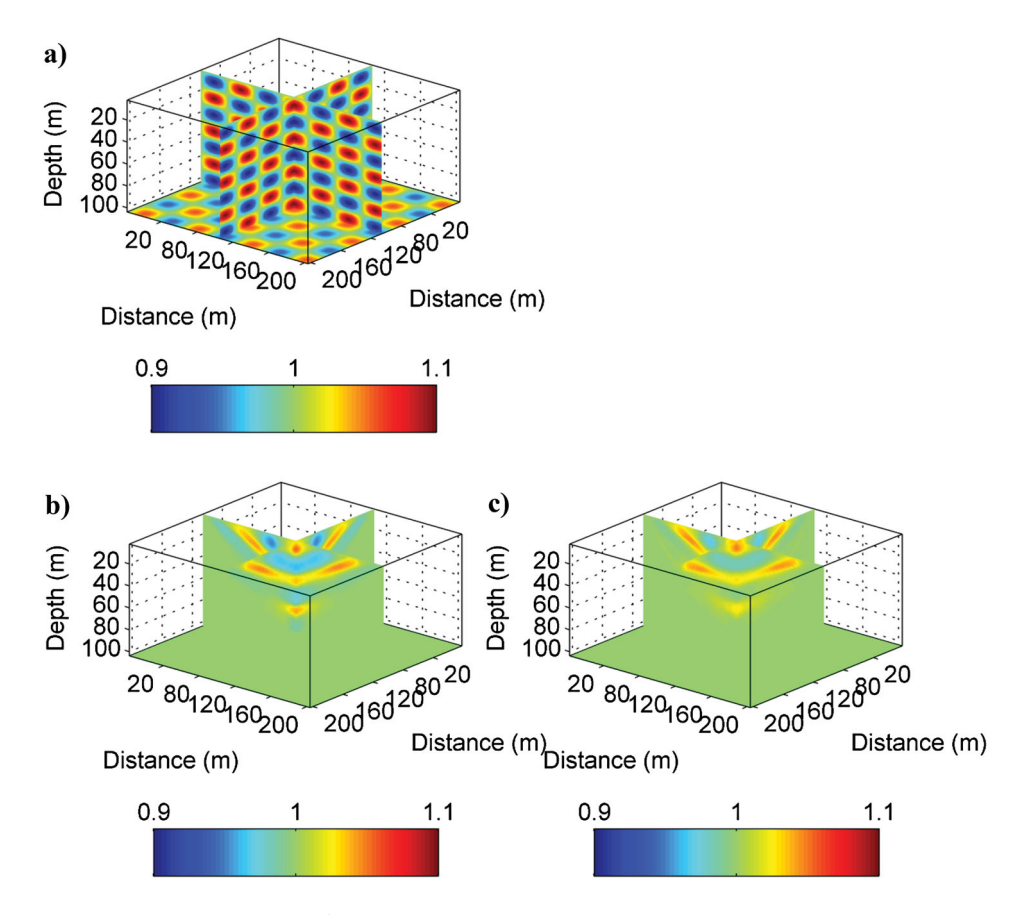


Figure 11. 3D inversion results comparison of S-wave. (a) S-wave checkerboard velocity model. (b) Inversion with 3D factored FSM. (c) Inversion with fdtime3d.c.

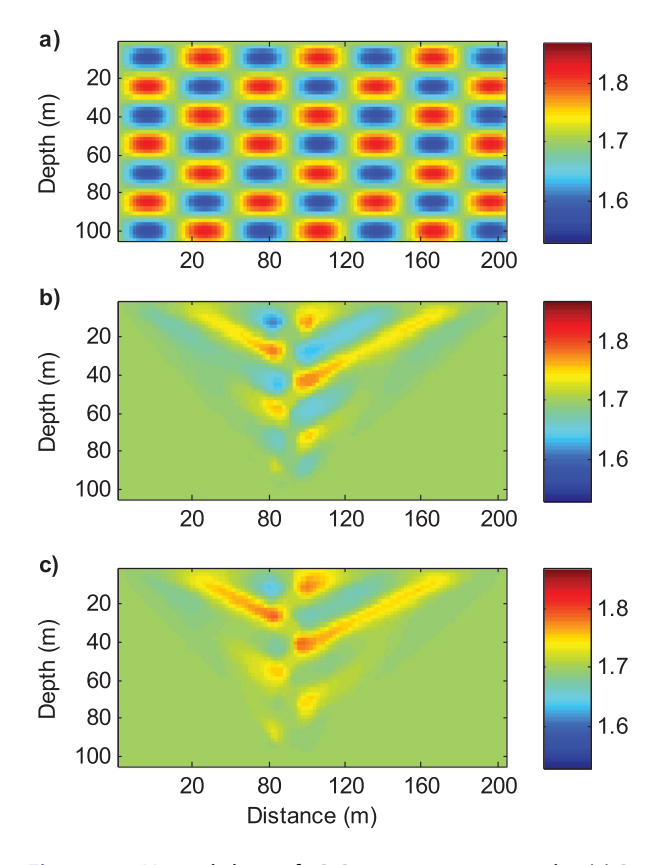


Figure 12. Vertical slices of 3D P-wave inversion results. (a) P-wave checkerboard velocity model. (b) Inversion with 3D factored FSM. (c) Inversion with *fdtime3d.c.*

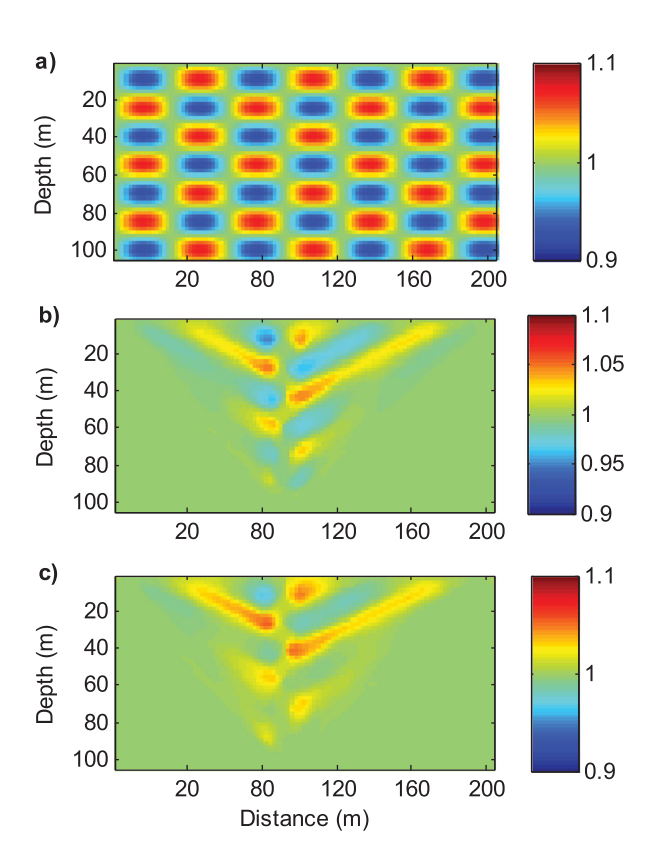


Figure 13. Vertical slices of 3D S-wave inversion results. (a) S-wave checkerboard velocity model. (b) Inversion with 3D factored FSM. (c) Inversion with *fdtime3d.c*.

We assume that

$$|\nabla T_0(\mathbf{x})|^2 = S_0^2(\mathbf{x}),\tag{10}$$

 T_0 and S_0 can both be calculated from an analytical solution. According to Equations (8) to (10), Equation (7) can be written as a factored eikonal equation (Fomel, Luo, and Zhao 2009):

$$T_0^2(\mathbf{x})|\nabla \tau(\mathbf{x})|^2 + 2T_0(\mathbf{x})\tau(\mathbf{x})\nabla T_0(\mathbf{x}) \cdot \nabla \tau(\mathbf{x})$$
$$+ [\tau^2(\mathbf{x}) - \alpha^2(\mathbf{x})]S_0^2(\mathbf{x}) = 0. \tag{11}$$

where $\alpha(\mathbf{x})$ is a constant or a variable.

The upwind finite-difference scheme is designed after discretising Equation (11) to follow the causality of the general eikonal equation. The numerical algorithm is presented on a 2D rectangular mesh. There are four grid points (A, B, C, D) around centre point O (Figure 1). We can discretise Equation (11) on the four triangles: ΔOAD , ΔOAB , ΔOBC and ΔOCD . Taking triangle ΔOBC as an example, the discretised equation can be written as:

$$T_0^2(O) \left| \left(\frac{\tau_O - \tau_B}{h}, \frac{\tau_O - \tau_C}{h} \right) \right|^2 + 2T_0(O)\tau_O \nabla T_0(O) \cdot \left(\frac{\tau_O - \tau_B}{h}, \frac{\tau_O - \tau_C}{h} \right) + [\tau_O^2 - \alpha^2(O)]S_0^2(O) = 0,$$
(12)

There may one or two real roots in Equation (12). If there is no real root in Equation (12), or these real roots cannot satisfy the causality condition, the method of characteristics can be used to pass information for τ from B to O and from C to O along edges \overrightarrow{BO} and \overrightarrow{CO} , respectively.

With $(\tau_x, \tau_y) = (p, q)$, the characteristic equation can be written as:

$$\begin{cases} \left(\frac{dx}{dt}, \frac{dy}{dt}\right) = (2T_0^2 p + 2\tau T_0 T_{0x}, 2T_0^2 q + 2\tau T_0 T_{0y}) \\ = 2T_0 \nabla T \\ \frac{d\tau}{dt} = 2T_0^2 (p^2 + q^2) + 2\tau T_0 (T_{0x} p + T_{0y} q) \\ = 2T_0 \nabla \tau \cdot \nabla T \end{cases}$$
(13)

 τ_{BO} and τ_{CO} can be calculated using the method of characteristics along two edges.

Fomel, Luo, and Zhao (2009) presented a local solver to calculate traveltimes. It uses a Gauss–Seidel iteration to sweep the whole computational domain with four alternating orderings, repeatedly. The detailed procedures of the factored FSM are given below.

- (1) Initialisation: assign the initial boundary condition for boundary grid points.
- (2) Gauss–Seidel iteration: execute four sweepings for the computational domain

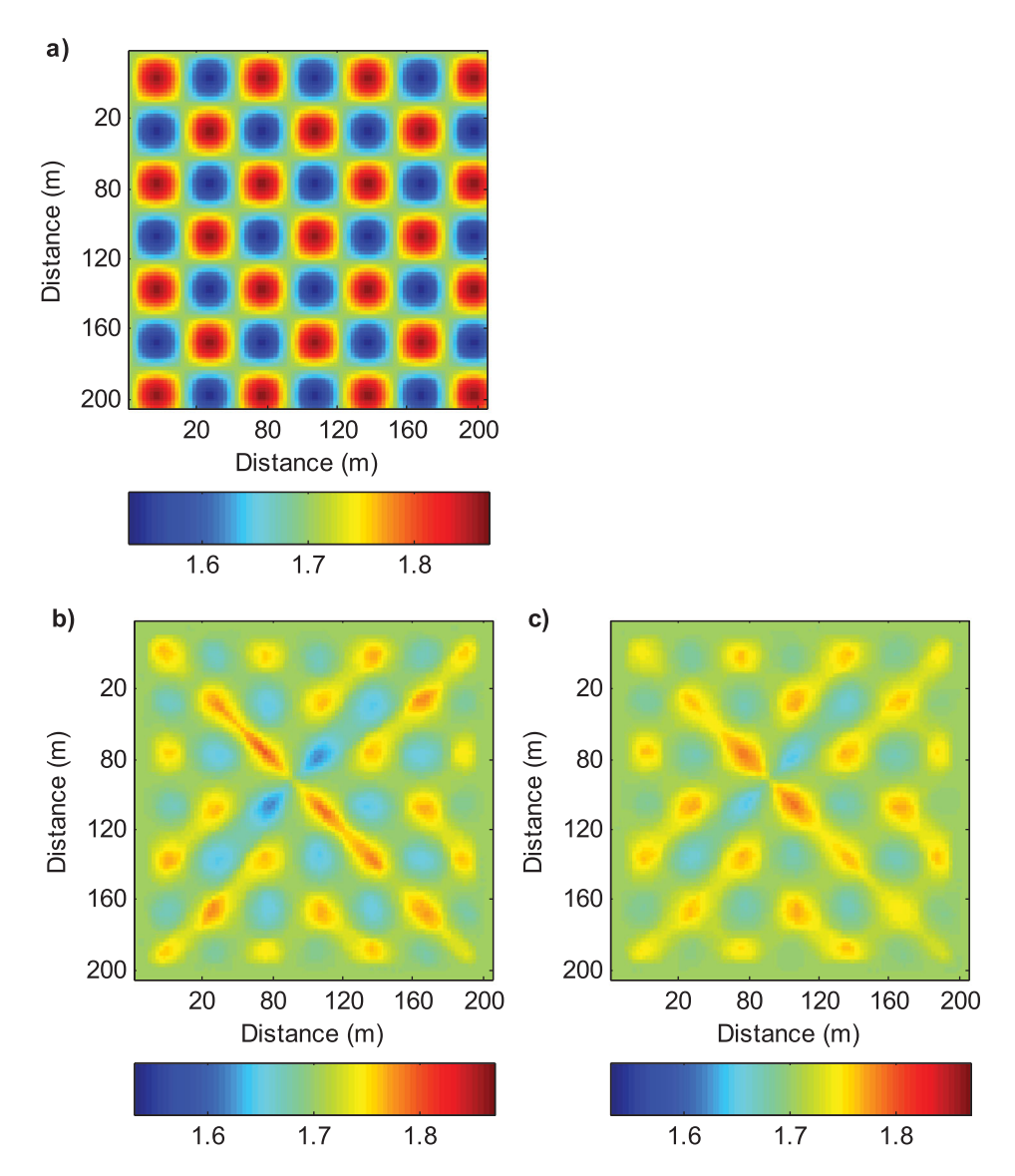


Figure 14. Horizontal slices of 3D P-wave inversion results (z = 8m). (a) P-wave checkerboard velocity model. (b) Inversion with 3D factored FSM. (c) Inversion with fdtime3d.c.

a.
$$i = 1: I, j = 1: J$$
 b. $i = 1: I, j = J: 1$
c. $i = I: 1, j = 1: J$ d. $i = I: 1, j = J: 1$

- (2.1) Discretise the factored eikonal equation on four triangles and calculate traveltimes. For example, solving Equation (12) for two real roots $\tau_{O,1}$ and $\tau_{O,2}$ on triangle $\triangle OBC$.
- (2.2) If two real roots $\tau_{O,1}$ and $\tau_{O,2}$ exist, then
 - if $\tau_{0,1}$ and $\tau_{0,2}$ satisfy the causality condition, choose the minimal traveltime $\tau_{BC} =$ $\min\{\tau_{O,1}T_0(O), \tau_{O,2}T_0(O)\};$
 - if only $\tau_{O,1}$ satisfies the causality condition, then $\tau_{BC} = \tau_{O,1} T_0(O)$;
 - if only $\tau_{0,2}$ satisfies causality condition, then $\tau_{BC} = \tau_{O,2} T_0(O)$.
- (2.3) If neither $\tau_{O,1}$ nor $\tau_{O,2}$ satisfy the causality condition, then calculate τ_{BO} and τ_{CO} using the method of characteristics. These two values should satisfy the causality condition $\tau_{BO}T_0(O) \geq T_B$ and $\tau_{CO}T_0(O) \geq T_C$, and choose $\tau_{BC} = \min\{\tau_{BO}T_0(O), \tau_{CO}T_0(O)\}.$

- (2.4) Repeat steps (2.1)–(2.3) for the remaining three triangles, and choose the smallest from the four traveltimes $T_O = \min$ $\{T_{DA}, T_{AB}, T_{BC}, T_{CD}\}.$
- (2.5) Calculate $\tau_{O} = T_{O}/T_{0}(O)$.

PStomo_eq package and its traveltime calculation algorithm

PStomo eq is a seismic traveltime tomographic open source package originally developed by Harley M. Benz (Benz et al. 1996). This package was modified by Tryggvason, Schmelzbach, and Juhlin (2009) for joint inversion of the P- and S-waves for local tomography. Velocity inversion of *PStome* eq is recalled briefly above. This package has been used widely in many applications (Tryggvason, Schmelzbach, and Juhlin 2009; Yordkayhun et al. 2009). Traveltime calculation algorithms (fdtime2d.c and fdtime3d.c) in the PStomo_eq

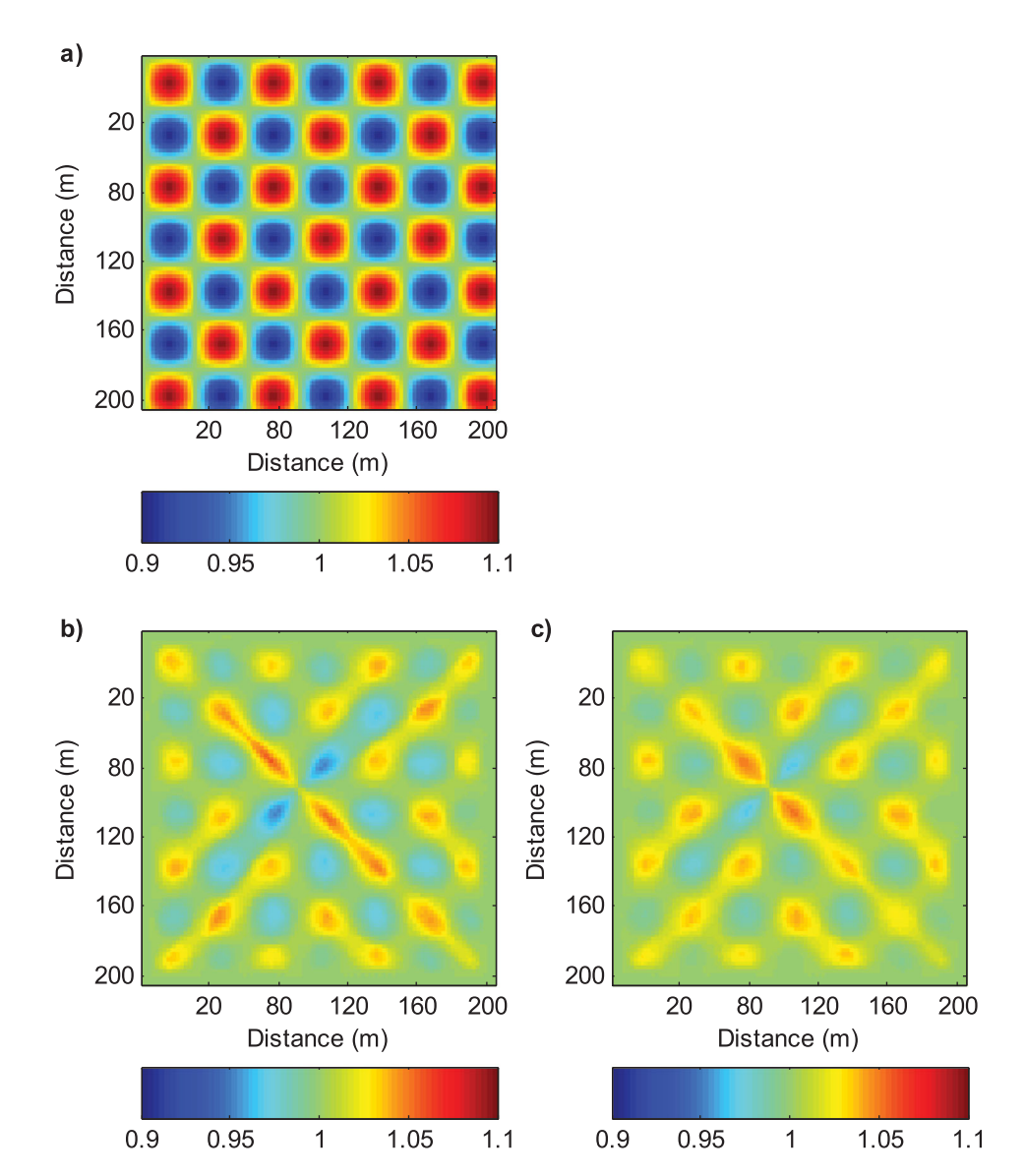


Figure 15. Horizontal slices of 3D S-wave inversion results (z=8m). (a) S-wave checkerboard velocity model. (b) Inversion with 3D factored FSM. (c) Inversion with *fdtime3d.c*.

package are provided by Podvin and Lecomte (1991). The two algorithms are modified slightly by Tryggvason and Bergman (2006). This method is based on a finite-difference approximation and Huygens principle. Different propagation modes (transmitted waves, diffracted body waves and head waves) are considered in the traveltime computation algorithm. Here, we recall the traveltime calculation method according to these three types of wavemodes (Figure 2).

First arrivals generated by transmission waves

When only points *Q* and *R* are timed, and the direction of wave propagation for point *O* is unknown, according to the eikonal equation, two estimates of the time gradient can be computed as:

$$\frac{\partial t}{\partial x} = \frac{t_R - t_Q}{h}, \quad \frac{\partial t}{\partial y} = \pm \sqrt{s^2 - \left(\frac{t_R - t_Q}{h}\right)^2}, \quad (14)$$

where h is mesh size, s is slowness in the cell defined by points Q, R and O. If the sign of $\partial t/\partial y$ is known, an estimate of arrival at point O can be computed. If point O is reached by this wavefront, then $0 \le (t_R - t_Q) \le hs/\sqrt{2}$; and if $\partial t/\partial y \ge 0$, then arrival time can be computed using the second term in Equation (14):

$$t_O = t_R + \sqrt{(hs)^2 - (t_R - t_Q)^2},$$
 (15)

There are eight traveltime estimates for the current point which should be computed according to 2D transmission waves.

First arrivals generated by head waves

s is the slowness of the current cell. If the slowness of the current cell is greater than slowness of the adjacent cell (s'), a head wave will be induced, travelling along edge RO. The arrival time at O can be computed by $t_O = t_R + hs'$. Therefore, a lower slowness value should be chosen for traveltime calculation. Arrival time for point O can be

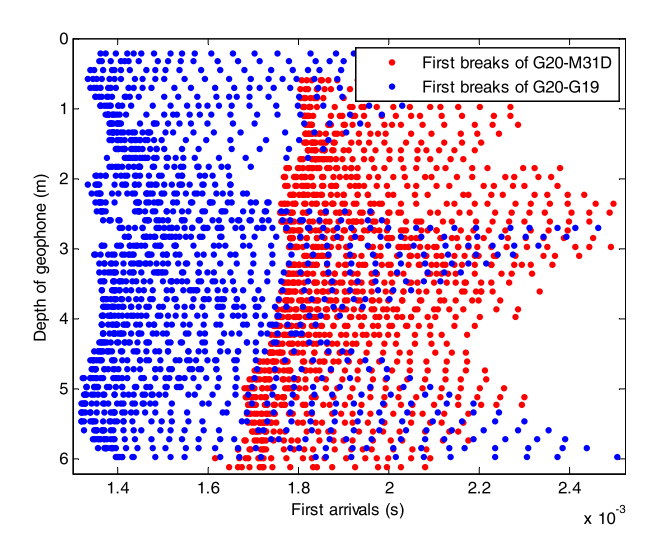


Figure 16. Distribution of first-arrivals vs. geophone depths.

expressed as:

$$t_O = t_R + h \min(s, s'), \tag{16}$$

in the 2D case, four different estimates of arrival time should be computed for the current point.

First arrivals generated by diffracted waves

Estimates of arrival time for point O are not reliable if only these two schemes are used when there is a local shadow zone in the current cell (see Figure 3). In fact, point Q can be considered a secondary source. It emits diffracted waves propagating through point O. On such an occasion, the arrival time at point O can be calculated by:

$$t_O = t_O + hs\sqrt{2}. (17)$$

in a 2D data structure, four estimates of arrival time should be computed for the current point.

Traveltime accuracy test

2D traveltime accuracy test

In this section, we test accuracy of factored FSM, FSM and fdtime2d.c on a 2D constant gradient velocity model to show the superiority of factored FSM. For a point source condition, there are analytical traveltimes for a certain velocity model. If the exact source location $\mathbf{x_0}$ is known, the slowness function can be written as:

$$\frac{1}{S(\mathbf{x})} = \frac{1}{S_0} + \mathbf{G_0} \cdot (\mathbf{x} - \mathbf{x_0}),\tag{18}$$

where S_0 is a constant value and $\mathbf{G_0}$ is constant gradient of velocity. The analytical traveltime can be written as (Fomel, Luo, and Zhao 2009):

$$T(\mathbf{x}) = \frac{1}{|\mathbf{G_0}|} \operatorname{arccos} h\left(1 + \frac{1}{2}S(\mathbf{x})S_0|\mathbf{G_0}|^2|\mathbf{x} - \mathbf{x_0}|^2\right),$$
(19)

where arccosh is an inverse hyperbolic cosine function

$$\arccos h(z) = \ln \left(z + \sqrt{z^2 - 1} \right). \tag{20}$$

Model parameters are given as:

- $\mathbf{x_0} = (0.0, 0.0);$
- the computational domain is $[0.0, 1.0] \times [0.0, 0.5]$
- mesh size is $0.00625 \, \text{km} \times 0.00625 \, \text{km}$;
- $S_0 = 2.0 \text{ s/km};$
- $\mathbf{G_0} = 1.0 \text{ 1/s}$, the constant gradient of velocity.

Figure 4 shows analytical traveltimes and traveltimes calculated by the factored FSM, FSM and fdtime2d.c algorithms. The time interval of the contour lines is 0.1 s. In order to better know the traveltime accuracy, traveltimes on a portion of the model (40×40 meshes) are shown in Figure 4(b). Traveltimes calculated by the factored FSM are much closer to the analytical solutions than that computed by FSM and fdtime2d.c in Figure 4(c).

Traveltime discrepancies between the analytical solution and numerical traveltimes are also made on 40×40 meshes (Figure 5). The maximal error between the analytical solution and traveltimes calculated by fdtime2d.c is 7.8e-3 s (Figure 5a). The maximal error between the analytical solution and traveltimes computed by the factored FSM is 9.8e-4s (Figure 5b). The ratio of these two errors can reach 7.9, and may become greater as the wave propagates further.

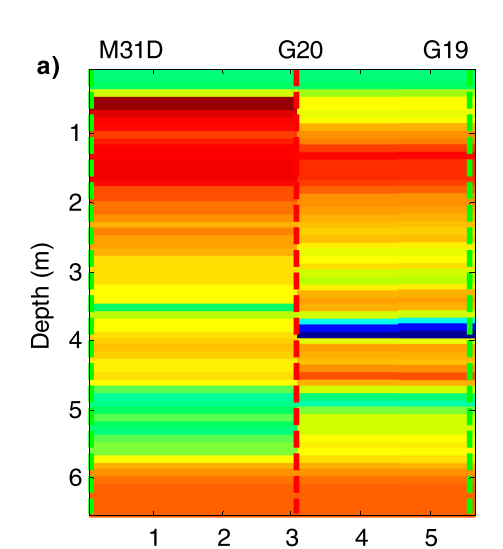
3D traveltime accuracy test

The 2D slowness model can be extended to the 3D case (Figure 6a), and can be used to test traveltime accuracy for 3D factored FSM, 3D FSM and fdtime3d.c.

Parameters for the 3D model set-up are:

- $\mathbf{x_0} = (0.0, 0.0, 0.0);$
- the computational domain is [0.0, 1.0] \times [0.0, 0.75] \times [0.0, 0.5] (km);
- cell size is $0.0125 \, \text{km} \times 0.0125 \, \text{km} \times 0.0125 \, \text{km}$;
- $S_0 = 2.0 \text{ s/km}$;
- $G_0 = 1.0 \text{ 1/s}.$

Figure 6(b) shows four iso-surfaces at 1.1 s for an analytical solution and traveltimes calculated by 3D factored FSM, 3D FSM and fdtime3d.c. From the vertical slice and the expanded map in Figure 6(c) and 6(d), we can see that traveltimes calculated by 3D factored FSM are much closer to the analytical solution than other traveltimes. Traveltime discrepancies are also found between the analytical solution and traveltimes computed by 3D factored FSM and fdtime3d.c. The maximal error between the analytical solution and



Distance (m)

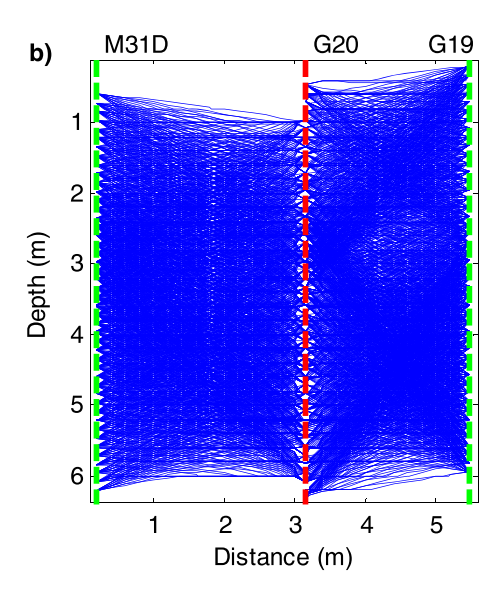


Figure 17. Initial velocity model and ray path distribution between wells (M31D–G20–G19). (a) Initial velocity model built using distances between shot and geophone in horizontal direction divided by its first-arrivals. (b) Ray path distribution between three wells.

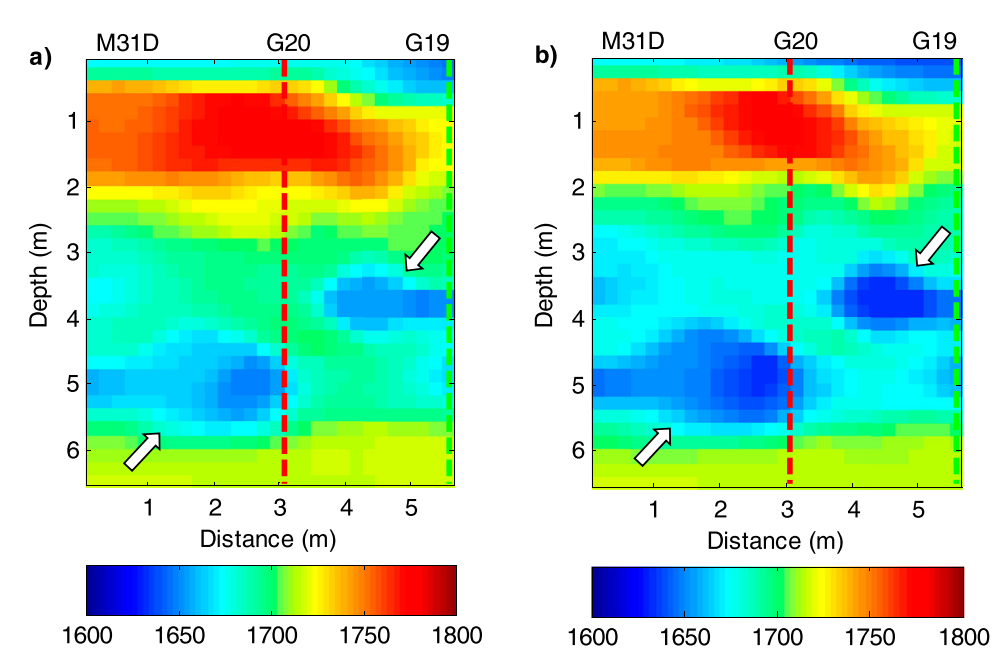


Figure 18. Inverted velocity profiles between three wells. (a) Inversion with fdtime2d.c. (b) Inversion with 2D factored FSM.

traveltimes calculated by *fdtime3d.c* is 0.0238. The maximal error between the analytical solution and traveltimes computed by 3D factored FSM is 0.0045395. The ratio between these two errors reaches 5.242. This suggests that traveltimes calculated by 3D factored FSM are more accurate than those calculated by *fdtime3d.c.* (Figure 7)

Numerical examples

2D checkerboard model reconstruction test

PStomo_eq incorporating 2D factored FSM and *fdtime2d.c* is used to invert a 2D checkerboard model. The model size is $104 \,\mathrm{m} \times 304 \,\mathrm{m}$ (Figures 8a and 9a). The size of the small checkers is $21 \,\mathrm{m} \times 20 \,\mathrm{m}$ at a depth

of 0–160 m. The size of big checkers is $34\,\text{m} \times 35\,\text{m}$ at a depth of 160–304 m. Velocity perturbation is 10% of the background model. The background velocity of the P-model is 1700 m/s and that of the S-model is 1000 m/s. Some 75 shots are distributed evenly on the left well with $\Delta S = 4$ m. Likewise, 75 receivers are distributed evenly on the right well with $\Delta R = 4$ m. Mesh size is $4 \, \text{m} \times 4 \, \text{m}$, and there are 1976 unknowns. However, there are 5625 source-receiver pairs. A specified level of Gaussian noise is added to synthetic traveltimes (noise level: 5% imes random imes $ar{\sigma}_{ob}$, where "random" is a numerical value in the range [-1 1], and $\bar{\sigma}_{ob}$ is the average variation of common shot gather traveltimes). The background model is taken as the initial velocity model. Parameters are the same for two inversions, when they incorporate factored FSM and fdtime2d.c, and both have

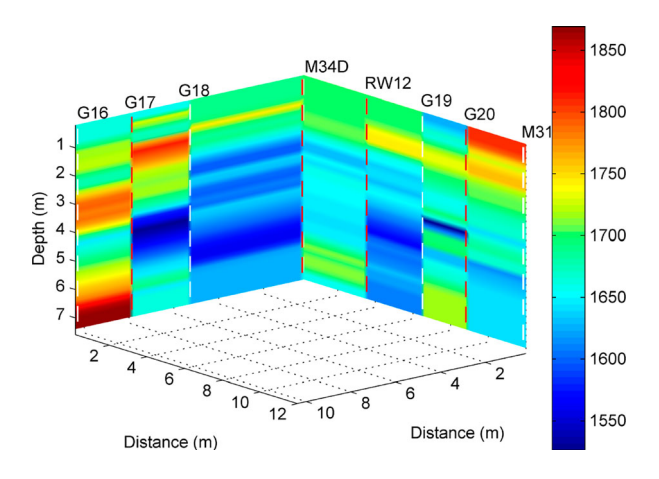


Figure 19. Initial velocity model for 2.5D traveltime inversion.

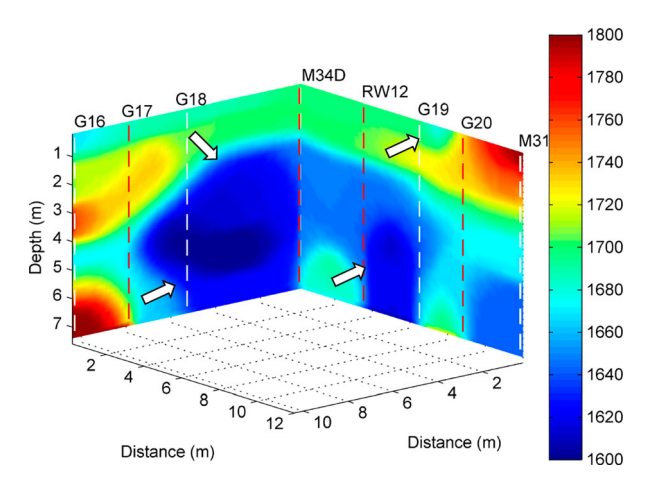


Figure 20. Velocity profile obtained by inversion with *fdtime3d.c.*

15 iterations for these two inversions. The results for a P-wave are shown in Figure 8(b) and 8(c), and the results for an S-wave are shown in Figure 9(b) and 9(c). Compared with the real model, the model recovered better when inversion incorporating factored FSM was used compared with inversion incorporating fdtime2d.c.

3D checkerboard model reconstruction test

PStomo_eq packages incorporating 3D factored FSM and fdtime3d.c are also used to invert a 3D checkerboard model. The model size is 204 m \times 204 m \times 104 m (Figures 10a and 11a). The size of the checkers is $30 \text{ m} \times 30 \text{ m} \times 15 \text{ m}$. Velocity perturbation is 10% of the background model, the background velocity of the P-model is 1700 m/s and that of the S- model is 1000 m/s. The shot well is located at (90 m, 90 m) on the surface. Some 51 shots are distributed evenly in the well with $\Delta S = 2 \,\mathrm{m}$, and 2500 receivers are distributed evenly on the surface with $\Delta Rx = \Delta Ry = 2$ m. Mesh size is $2 \text{ m} \times 2 \text{ m} \times 2 \text{ m}$, and there are 541,008 unknowns. There are 127,500 source-receiver pairs. Likewise, 5% Gaussian noise is added into synthetic traveltimes. Homogeneous models with 1700 and 1000 m/s are taken as initial P- and S-wave velocity models,

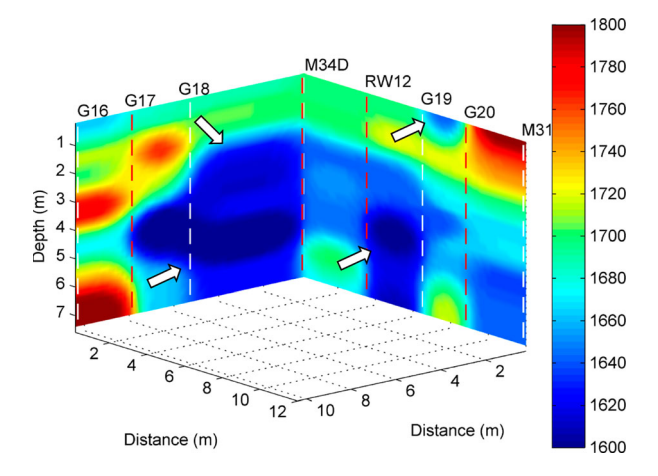


Figure 21. Velocity profile obtained by inversion with 3D factored FSM.

respectively. All input parameters are the same for the two inversions. After 15 iterations for the two inversions, the P- and S- wave results shown in Figure 10(b) and 10(c), and Figure 11(b) and 11(c) are obtained. Checkers with a low velocity obtained by inversion with factored FSM are much clearer than those obtained by inversion with fdtime3d.c. Vertical and horizontal slices of the tomograms are shown in Figures 12–15. Figures 12 and 13 are vertical slices of the models. In the vicinity of the shot well, checkers obtained by inversion with factored FSM are much clearer. Figures 14 and 15 are horizontal slices of the models (z=8 m). Again, checkers obtained by inversion with factored FSM are much clearer.

Field data from a water-contaminated site Field data test: 2D case

Velocity inversions with 2D factored FSM and fdtime2d.c are applied to a field data set. The field site is near an electric power plant in Pinellas County, Florida, USA. This investigation is to analyse contaminated liquid distribution underground. Three wells (M31D, G20 and G19) are selected for the traveltime inversion. M31D, G20 and G19 are located at x = 0.2, 3.17 and 5.47 m, respectively. G20 is a shot well, M31D and G19 are receiver wells. Mesh size for this computational domain is 56×64 with a cell size of $2 \text{ m} \times 2 \text{ m}$. The number of unknowns is 896. There are 2798 source-receiver pairs. The curve between first-arrivals and the depth of geophones is shown in Figure 16. If the initial model is much closer to the real model, inversion convergence is faster and easier. However, if the initial model differs greatly from the real model, the inversion result also differs greatly from real model (Kissling et al. 1994; Liu et al. 2010). Therefore, the initial model in this inversion is built using the horizontal distance between the shot and geophone divided by its first-arrival. The initial velocity model is shown in Figure 17(a). Ray path distribution is shown in Figure 17(b) after 20 inversion iterations. A previous study showed that the strata

between these three wells are mildly polluted (Ajo-Franklin, Urban, and Harris 2006). Figure 18 shows results of inversion incorporating factored FSM and fdtime2d.c. There are two apparent low-velocity zones (see areas marked by arrow notation), which are much clearer in Figure 18(b) than in Figure 18(a).

Field data test: 2.5D case

Velocity inversion with 3D factored FSM and fdtime3d.c is also applied to the same field data set. Eight wells (G16, G17, G18, M34D, RW12, G19, G20 and M31D) are used to join traveltime inversion. There are four shot wells (G17, M34D, RW12 and G20) and five receiver wells (G16, G18, M34D, G19 and M31D). Among them, M34D is both a shot well and a receiver well. The 2.5D initial velocity model is built using the horizontal distance between the shot and geophone divided by its firstarrival. The initial model is shown in Figure 19. Velocity profiles obtained by inversion with 3D factored FSM and fdtime3d.c are shown in Figures 20 and 21. There are many low-velocity anomalies, which may be caused by contaminated liquid. Areas marked by arrows are much clearer in Figure 21 than in Figure 20. Contaminated liquid diffuses and migrates laterally along the strata and accumulates in some unconsolidated deposits.

Conclusions

First-arrival tomography incorporating 2D and 3D factored FSMs is presented. The factored FSM can deal with the source singularity problem for a point source condition. Therefore, it can generate more accurate traveltimes than other finite-difference based eikonal solvers. The traveltime computation method has a significant role in first-arrival tomography. A robust and accurate traveltime computation method can improve the tomographical result to a certain extent. Traveltimes of P- and S-waves are incorporated in the regularisation equation. In 2D and 3D checkerboard model reconstruction tests, the results obtained by inversion with factored FSM are much clearer than those inverted by the PStomo eq package. Velocity inversion is performed for a field data set in water-contaminated land to delineate areas polluted by toxic liquid. In the 2D and 2.5D cases, the results obtained by inversion with factored FSM delineate any velocity anomalies more clearly. Lowvelocity zones may be caused by toxic liquid that diffuses and migrates along strata, and finally deposits in some unconsolidated formations.

Acknowledgements

The authors greatly appreciate Dr. Jonathan B. Ajo-Franklin in Lawrence Berkeley National Laboratory kindly provided the first arrival data, and coordinates of shots and geophones in real data test.

Disclosure statement

No potential conflict of interest was reported by the authors.

Funding

This research is jointly supported by National Natural Science Foundation of China (41504095, 41764006), Foundation of Education Department in Jiangxi (GJJ160570), and China Scholarship Council. Dr Luo was partially supported by NSF Division of Mathematical Sciences 1418908 and 1719907.

References

- Ajo-Franklin, J. B., J. A. Urban, and J. M. Harris. 2006. Using resolution-constrained adaptive meshes for traveltime tomography. Journal of Seismic Exploration 14: 371-92.
- Aki, K., and W. H. K. Lee. 1976. Determination of threedimensional velocity anomalies under a seismic array using first P arrival times from local earthquakes: 1. A homogeneous initial model. Journal of Geophysical Research 81: 4381-99. DOI:10.1029/JB081i023p04381.
- Benz, H. M., B. A. Chouet, P. B. Dawson, J. C. Lahr, and R. A. Page. 1996. Three-dimensional P and S wave velocity structure of Redoubt Volcano, Alaska. Journal of Geophysical Research: Solid Earth 101, no. B4: 8111-28. DOI:10.1029/95JB03 046.
- Bergman, B., A. Tryggvason, and C. Juhlin. 2004. Highresolution seismic traveltime tomography incorporating static corrections applied to a till-covered bedrock environment. Geophysics 69, no. 4: 1082-90. DOI:10.1190/1.177
- Calvert, A. J., and M. A. Fisher. 2001. Imaging the Seattle Fault Zone with high-resolution seismic tomography. Geophysical Research Letters 28: 2337-40. DOI:10.1029/2000GL0
- Cerveny, V. 2001. Seismic ray theory. Cambridge: Cambridge University Press, DOI:10.1115/1.1508173.
- Cheng, N., and L. House. 1996. Minimum traveltime calculation in 3-D graph theory. Geophysics 61: 1895-8. DOI:10.1190/1.1444104.
- Engdahl, E. R., R. V. D. Hilst, and R. Buland. 1998. Global teleseismic earthquake relocation with improved travel times and procedures for depth determination. Bulletin of the Seismological Society of America 88, no. 3: 722–43.
- Ettrich, N., and D. Gajewski. 1996. Wave front construction in smooth media for prestack depth migration. Pure and Applied Geophysics 148, no. 3: 481–502. DOI:10.1007/BF008 74576.
- Fischer, R., and J. M. Lees. 1993. Shortest path ray tracing with sparse graphs. Geophysics 58, no. 7: 987-96. DOI:10.1190/ 1.1443489.
- Fomel, S., S. T. Luo, and H. K. Zhao. 2009. Fast sweeping method for the factored eikonal equation. Journal of Computational Physics 228, no. 17: 6440-55. DOI:10.1016/j.jcp. 2009.05.029.
- Han, S., W. Zhang, and J. Zhang. 2017. Calculating qP-wave travel times in 2D TTI media by high-order fast sweeping method with a numerical quartic equation solver. Geophysical Journal International 210, no. 3: 1560-69. DOI:10.1093/gji/ggx236.
- Huang, G. N., B. Zhou, H. X. Li, and D. C. Nobes. 2017. Seismic traveltime inversion based on tomographic equation without integral terms. Computer & Geosciences 104: 29-34. DOI:10.1016/j.cageo.2017.04.002.



- Huang, G. N., B. Zhou, H. X. Li, H. Zhang, and Z. L. Li. 2014. 2D seismic reflection tomography in strongly anisotropic media. Journal of Geophysics and Engineering 11: 1-8. DOI:10.1088/1742-2132/11/6/065012.
- Hole, J. A., and B. C. Zelt. 1995. 3-D finite-difference reflection traveltimes. Geophysical Journal International 121: 427–34. DOI:10.1111/j.1365-246X.1995.tb05723.x.
- Kennett, B. L. N., E. R. Engdahl, and R. Buland. 1995. Constraints on seismic velocities in the Earth from traveltimes. Geophysical Journal International 122: 108–24. DOI:10.1111/j.1365-246X.1995.tb03540.x.
- Kim, S., and R. Cook. 1999. 3-D traveltime computation using second-order ENO scheme. Geophysics 64: 1867–76. DOI:10.1190/1.1444693.
- Kissling, E., W. L. Ellsworth, D. Eberhart-Phillips, and U. Kradolfer. 1994. Initial reference models in local earthquake tomography. Journal of Geophysical Research: Solid Earth 99, no. B10: 19635-46. DOI:10.1029/93JB03138.
- Lambare, G., P. S. Lucio, and A. Hanyga. 1996. Two-dimensional multivalued traveltime and amplitude maps by uniform sampling of a ray field. Geophysical Journal International 125: 584-98. DOI:10.1111/j.1365-246X.1996.tb 00021.x.
- Lees, J. M. 1992. The magma system of Mount St. Helens non-linear high-resolution P-wave tomography. Journal of Volcanology and Geothermal Research 53: 103–16. DOI:10. 1016/0377-0273(92)90077-Q.
- Lees, J. M., and R. S. Crosson. 1989. Tomographic inversion for three-dimensional velocity structure at Mount St. Helens using earthquake data. Journal of Geophysical Research 94, no. B5: 5716-28. DOI:10.1029/JB094iB05p05716.
- Leidenfrost, A., N. Ettrich, D. Gajewski, and D. Kosloff. 1999. Comparison of six different methods for calculating travel times. Geophysical Prospecting 47: 269-97. DOI:10.1046/j.1365-2478.1999.00124.x.
- Liu, Y. Z., K. Y. Ding, and L. G. Dong. 2010. The dependence of first-arrival travel time tomography on initial model. Oil Geophysical Prospecting 45, no. 4: 502–11.
- Luo, S. T., and J. L. Qian. 2011. Factored singularities and high-order Lax-Friedrichs sweeping schemes for pointsource traveltimes and amplitudes. Journal of Computational Physics 230: 4742-55. DOI:10.1016/j.jcp.2011. 02.043.
- Luo, S., and J. Qian. 2012. Fast sweeping methods for factored anisotropic eikonal equations: Multiplicative and additive factors. Journal of Scientific Computing 52: 360-82. DOI:10.1007/s10915-011-9550-y.
- Marti, D., R. Carbonell, and I. Flecha. 2008. High-resolution seismic characterization in an urban area: Subway tunnel construction in Barcelona, Spain. *Geophysics* 73, no. 2: B41–50. DOI:10.1190/1.2832626.
- Moser, T. J. 1991. Shortest path calculation of seismic rays. Geophysics 56, no. 1: 59-67. DOI:10.1190/1.1442958.
- Nakanishi, I., and K. Yamaguchi. 1986. A numerical experiment of nonlinear image reconstruction from first-arrival times for two-dimensional island arc structure. Journal of Physics of the Earth 34: 195-201. DOI:10.4294/jpe1952. 34.195.
- Nolet, G. 2008. A breviary of seismic tomography imaging the interior of the Earth and Sun. Cambridge: Cambridge University Press, DOI:10.1121/1.3203995.
- Podvin, P., and I. Lecomte. 1991. Finite difference computation of traveltimes in very contrasted velocity models: A massively parallel approach and its associated tools. Geophysical Journal International 105: 271-84. DOI:10.1111/j.1365-246X.1991.tb03461.x.

- Phillips, W. S., and M. C. Fehler. 1991. Traveltime tomography: A comparison of popular methods. Geophysics 56, no. 10: 1639-49. DOI:10.1190/1.1442974.
- Qian, J., and W. W. Symes. 2001. Paraxial eikonal solvers for anisotropic quasi-P travel times. Journal of Computational Physics 173: 256-78. DOI:10.1006/jcph.2001.6875.
- Qian, J., and W. W. Symes. 2002a. Finite-difference quasi-P traveltimes for anisotropic media. Geophysics 67: 147-55. DOI:10.1190/1.1451438.
- Qian, J., and W. W. Symes. 2002b. An adaptive finite-difference method for traveltimes and amplitudes. Geophysics 67, no. 1: 167-76. DOI:10.1190/1.1451472.
- Qin, F. H., Y. Luo, and K. B. Olsen. 1992. Finite-difference solution of the eikonal equation along expanding wavefronts. Geophysics 57, no. 3: 478-87. DOI:10.1190/1.1443263.
- Rawlinson, N., and S. Fishwick. 2012. Seismic structure of the southeast Australian lithosphere from surface and body wave tomography. Tectonophysics 572-573: 111-22. DOI:10.1016/j.tecto.2011.11.016.
- Sethian, J., and M. Popovici. 1999. 3-D traveltime computation using the fast-marching method. Geophysics 64, no. 2: 516-23. DOI:10.1190/1.1444558.
- Toomey, D. R., S. C. Solomon, and G. M. Purdy. 1994. Tomographic imaging of the shallow crustal structure of the East Pacific Rise at 9° 30′N. Journal of Geophysical Research: Solid Earth 99, no. B12: 24135-57. DOI:10.1029/94JB01942.
- Tryggvason, A., and B. Bergman. 2006. A traveltime reciprocity discrepancy in the Podvin & Lecomte time3d finite difference algorithm. Geophysical Journal International 165: 432-5. DOI:10.1111/j.1365-246X.2006.02925.x.
- Tryggvason, A., S. T. Rognvaldsson, and O. G. Flovenz. 2002. Three-dimensional imaging of the P- and S-wave velocity structure and earthquake locations beneath southwest Iceland. Geophysical Journal International 151:848-66. DOI:10.1046/j.1365-246X.2002.01812.x.
- Tryggvason, A., C. Schmelzbach, and C. Juhlin. 2009. Traveltime tomographic inversion with simultaneous static corrections — well worth the effort. Geophysics 74, no. 6: WCB25-33. DOI:10.1190/1.3240931.
- Tsai, Y. H., L. T. Cheng, S. Osher, and H. K. Zhao. 2003. Fast sweeping algorithms for a class of Hamilton-Jacobi equations. SIAM Journal on Numerical Analysis 41, no. 2: 673–94. DOI:10.1137/S0036142901396533.
- Van Trier, J., and W. W. Symes. 1991. Upwind finite-difference calculation of travel times. Geophysics 56, no. 6: 812-21. DOI:10.1190/1.1443099.
- Vesnaver, A. L., F. Accaino, G. Bohm, and G. D. Moro. 2003. Time-lapse tomography. Geophysics 68, no. 3: 815-23. DOI:10.1190/1.1581034.
- Vidale, J. 1988. Finite-difference calculation of travel times. Bulletin of the Seismological Society of America 78, no. 6: 2062-76.
- Vidale, J. 1990. Finite-difference calculation of traveltimes in three dimensions. Geophysics 55, no. 5: 521-6. DOI:10.1190/ 1.1442863.
- Vinje, V., K. Astebol, E. Iversen, and H. Gjoystdal. 1999. 3-D ray modeling by wavefront construction in open models. Geophysical Prospecting 64: 1912-19. DOI:10.1190/1.144
- Vinje, V., E. Iversen, and H. Gjoystdal. 1993. Traveltime and amplitude estimation using wavefront construction. Geophysics 58: 1157-66. DOI:10.1190/1.1443499.
- Waheed, U., and T. Alkhalifah. 2017. A fast sweeping algorithm for accurate solution of the tilted transversely isotropic eikonal equation using factorization. Geophysics 82, no. 6: WB1-8. DOI:10.1190/geo2016-0712.1.



- Yordkayhun, S., A. Tryggvason, B. Norden, C. Juhlin, and B. Bergman. 2009. 3D seismic travel time tomography imaging of the shallow subsurface at the CO2SINK project site, Ketzin, Germany. Geophysics 74, no. 1: G1-15. DOI:10.1190/ 1.3026553.
- Zelt, C. A., A. Azaria, and A. Levander. 2006. 3D seismic refraction traveltime tomography at a groundwater contamination site. *Geophysics* 71: H67–78. DOI:10.1190/1.2258094.
- Zhao, H. K. 2005. A fast sweeping method for eikonal equations. Mathematics of Computation 74, no. 250: 603-28. DOI:10.1.1.153.6742.
- Zhou, H. W. 2006. First-break vertical seismic profiling tomography for Vinton Salt Dome. Geophysics 71, no. 3: U29-36. DOI:10.1190/1.2192970.
- Zhou, B., and S. A. Greenhalgh. 2006. Raypath and traveltime computations for 2D transversely isotropic media with dipping symmetry axes. Exploration Geophysics 37, no. 2: 150-9. DOI:10.1071/EG06150.
- Zhou, B., C. Sinadinovski, and S. A. Greenhalgh. 1992. Nonlinear inversion travel-time tomography: Imaging highcontrast inhomogeneities. Exploration Geophysics 23, no. 2: 459-64. DOI:10.1071/EG992459.